Nanoscale

PAPER

View Article Online
View Journal | View Issue

Cite this: *Nanoscale*, 2018, **10**, 3254

Achieving rapid Li-ion insertion kinetics in TiO_2 mesoporous nanotube arrays for bifunctional high-rate energy storage smart windows†

Zhongqiu Tong,‡[a,b] Shikun Liu,‡[c] Xingang Li,[d] Liqiang Mai,*[e] Jiupeng Zhao[c] and Yao Li*[b]

Smart electrochromic windows integrated with electrochemical energy storage capacity are receiving increasing interest for green buildings. However, the fabrication of bifunctional devices that demonstrate high-rate capability with stable and desirable optical modulation still remains a great challenge. Herein, a facile sacrificial template-accelerated hydrolysis approach is presented to prepare a designed lithium-ion insertion-type material layer on a fluorine-doped tin oxide substrate, with TiO_2 mesoporous nanotube array (MNTA) film as an example, with rapid Li-ion insertion kinetics and without sacrificing window transparency, to meet requirements. A bifunctional device is assembled to exhibit the optical-electrochemical superiority of MNTA nanostructures. The as-assembled bifunctional smart window exhibits strong electrochromic contrast and high-rate capability in the fast galvanostatic charge/discharge process. For instance, at 1 A g^{-1}, it completes the charge or discharge process within only 232 s and delivers a high, reversible and stable specific capacity of 60 mA h g^{-1}, accompanying obvious transmittance modulation in the visible spectrum, with a typical value of *ca.* 30.4% at 700 nm, and strong color changes between deep blue and transparency.

Received 16th October 2017,
Accepted 16th January 2018

DOI: 10.1039/c7nr07703c

rsc.li/nanoscale

1. Introduction

Energy saving and storage are becoming more and more urgent due to pressing issues, such as global warming, the energy crisis, and resultant environmental concerns.[1] In line with these worldwide efforts, the use of bifunctional devices integrating electrochromic glass and energy storage is attractive because of their promising properties, such as efficient sun shading, which decreases the cost of air conditioning, being an accessible power source everywhere in green energy-effective buildings, their ability to provide comfortable esthetic decoration, and their smart space-utilization.[2–9] Steiner *et al.* fabricated an electrochromic supercapacitor with a double-gyroid V_2O_5 network.[10] Wei *et al.* used ordered polyaniline nanowire array electrodes to build a capacitive energy storage electrochromic device.[11] Mai *et al.* reported WO_3 films for pseudocapacitive glass windows.[12] These devices simultaneously exhibited electrochemical energy storage properties and acceptable transmittance modulation during the galvanostatic charge/discharge process. But bifunctional devices with higher energy density are ready to be exploited to meet practical applications when used as power sources.[7–9] Recently, a self-powered and self-rechargeable aqueous electrochromic battery operating through the mechanism of the difference in work functions between Prussian blue and aluminium was presented by Wang *et al.*[13] But its specific capacity was unsatisfactory, and the battery device needed a long self-charging time (corresponding to the coloration process). Zhao *et al.* broke these two barriers by adding trace amount of H_2O_2 into the electrolyte to accelerate the charging process, leading to improved specific capacity and a fast charging response.[14] However, such aqueous electrochromic batteries also have to face the insurmountable obstacles of side reactions between aluminium and water or H_2O_2, leading these devices to exhibit poor cycling and storage stability. Thus far, it is still an urgent requirement to fabricate bifunctional electrochromic devices

[a]*School of Materials Science and Engineering, Southwest Petroleum University, Chengdu 610500, China*
[b]*Center for Composite Materials and Structure, Harbin Institute of Technology, Harbin 150001, China. E-mail: yaoli@hit.eu.cn*
[c]*School of Chemistry and Chemical Engineering, Harbin Institute of Technology, Harbin 150001, China*
[d]*China Construction Fourth Engineering Division Corp. LTD, Guangzhou 510000, China*
[e]*State Key Laboratory of Advanced Technology for Materials Synthesis and Processing, Wuhan University of Technology, Wuhan 430070, Hubei, China. E-mail: mlq518@whut.edu.cn*

†Electronic supplementary information (ESI) available. See DOI: 10.1039/c7nr07703c

‡These two authors contributed equally to this work.

that can exhibit high energy density accompanying stable and fast optical modulation.

The fabrication of electrochromic energy storage devices with ion insertion-type transition metal oxides enables them to deliver high energy density.[7,8] Nevertheless, the ion insertion process in the bulk is rather sluggish, giving rise to poor rate capability, low transmittance modulation, and a slow coloration/bleaching response.[7–9] To build an electroactive material layer with fast ion-insertion kinetics possessing high energy and power capacities, as well as a desirable electrochromic response, strategies to ameliorate metal oxides are generally focused on the following aspects: (i) architectural design with favorable electronic and/or ion diffusion, as well as reductions in electron and ion diffusion path lengths; and (ii) improving the surface redox contribution to the total ion insertion reactions, referred to as the pseudocapacitive effect. Mesoporous nanotube array (MNTA) film electrodes are considered as one type of the most promising candidates to fabricate bifunctional electrochromic devices, owing to their high electrode/electrolyte contact areas, their short electron and ion diffusion distances, them having enough space for volume expansion,[7,15] and, more importantly, their underlying accelerated ion insertion rates and the appearance of the pseudocapacitive effect derived from high surface redox contributions.[8,16–18]

In this work, we present transparent metal oxide MNTA films directly grown on fluorine-doped tin oxide (FTO) substrates with high specific energy and power densities for bifunctional smart windows. Titanium dioxide (TiO_2), a typical insertion-type metal oxide widely used for electrochromism[19] and Li-ion batteries (anode material)[20] but suffering from slow Li-ion insertion,[16,21] is selected as the prototype. To prepare TiO_2 mesoporous nanotube arrays strongly attached to the FTO substrates, a sacrificial template-accelerated hydrolysis (STAH) approach is employed, using ZnO nanorod arrays as the templates.[22] The merit of such a slow hydrolysis process is that it leads the mesoporous nanotubes to be constructed from random stacks of several nanometer-sized TiO_2 crystals.[23] A bifunctional energy storage smart window was assembled using a pair of electrodes made of FTO substrates, each coated with an equal area of TiO_2 MNTAs. By virtue of their structural features, the TiO_2 MNTAs show rapid Li-ion insertion kinetics, leading to the assembled device exhibiting high-rate capability as well as a state-of-the-art color switching speed compared to other reported electrochromic energy storage devices.

2. Experimental section

2.1. Fabrication of TiO_2 mesoporous nanotube arrays (MNTAs)

The synthesis process for TiO_2 MNTAs is illustrated in Fig. 1a. Electrodeposited ZnO nanorod arrays on FTO substrates are used as the templates.[24] Before electrodeposition, the FTO substrates (9 Ω cm^{-2}) were cleaned ultrasonically in acetone, in methanol, and then in distilled water, for 20 min each. ZnO nanorod arrays were grown on the FTO substrate in an aqueous electrolyte containing 0.02 M $Zn(NO_3)_2$, 0.01 M ammonium acetate and 0.01 M hexamethylenetetramine, with a current density of 0.5 mA cm^{-2} at 90 °C for 40 min. After being rinsed with ethanol and then pure water, the ZnO templates were annealed at 350 °C for 3 h in air to enhance the mechanical stability.

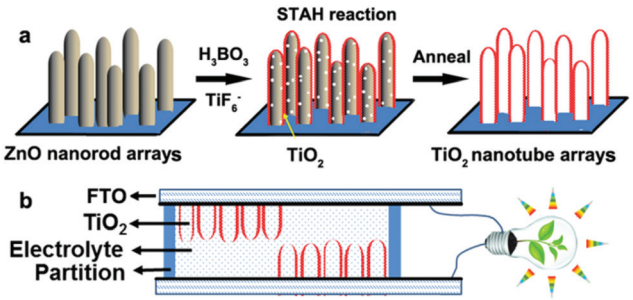

Fig. 1 (a) A schematic diagram of the formation process of TiO_2 MNTAs. (b) A schematic illustration of the bifunctional device.

TiO_2 mesoporous nanotube arrays were synthesized *via* a facile STAH process using the above prepared ZnO templates. In a typical process, the as-prepared ZnO nanorod arrays on FTO substrates were immersed in an aqueous solution consisting of 0.075 M $(NH_4)_2TiF_6$ and 0.2 M H_3BO_3 at room temperature for 30 min. In this solution, the slow hydrolysis reactions occurring between TiF_6^{2-} and H_3BO_3 produced TiO_2 nanoparticles and other soluble products (BF_4^-, and H_3O^+ ions); meanwhile, the ZnO nanorods gradually dissolved in the acidic environment, as shown in the following equations:[22,23]

$$TiF_6^{2-} + 2H_2O \leftrightarrow TiO_2 + 6F^- + 4H^+ \quad (1)$$

$$H_3BO_3 + 4F^- + 4H^+ \leftrightarrow BF_4^- + H_3O^+ + 2H_2O \quad (2)$$

$$ZnO + 2H_3O^+ \rightarrow Zn^{2+} + 3H_2O. \quad (3)$$

Then, the samples were washed with distilled water and annealed at 420 °C for 3 h in air. The loading mass density was about 0.15 mg cm^{-2}.

2.2. Assembly of the electrochromic device and energy storage smart window

An electrochromic cell was assembled through capping MNTA film with an FTO counter electrode, using a precut thermoplastic gasket as a spacer, infiltrating this with 1 M $LiClO_4$ in propylene carbonate, inserting an Ag/AgCl wire as the reference electrode, and then sealing the device with epoxy glue.

The energy storage smart window was assembled in the same manner employed to build the electrochromic device, but without inserting the Ag/AgCl wire, and replacing the FTO substrate with TiO_2 MNTAs. The device was assembled with a pair of electrodes made of FTO substrates, each coated with an equal area of TiO_2 MNTAs (Fig. 1b).

2.3. Characterization

The morphologies, crystalline structures, and UV-vis optical properties of the samples were characterized *via* scanning elec-

tron microscopy (SEM, FEI Helios Nanolab 600i), X-ray diffraction with Cu Kα radiation (XRD, Bruker AXS D2 Phaser), transmission electron microscopy (TEM, FEI Tecnai G2F30, 300 kV), high-resolution TEM (HRTEM, FEI), selected area electron diffraction (SAED), Raman scattering (JY Co. LABRAM-HR), and UV-vis spectrophotometry (PerkinElmer, Lamda950).

The electrochemical properties were evaluated using a nitrogen-filled three-electrode cell with an electrochemical analyzer (CHI 660D, Shanghai Chenhua Instrument Co. Ltd) in 1 M $LiClO_4$/propylene carbonate (PC). The reference electrode was an Ag/AgCl wire in saturated LiCl dissolved in anhydrous acetonitrile. A platinum plate was employed as the counter electrode. *In situ* electrochromic measurements of the TiO_2 MNTAs were performed using an experimental cell produced in-house (with the same setup as used in ref. 15). The experimental cell was sealed in an argon-filled glove box (Vigor Glove Box, Suzhou, China) before testing. One side of the setup was connected to a white lamp (DT-mini-2-GS, Ocean Optics) *via* an optical fiber; the other side was connected to an optical spectrometer (MAYA 2000-Pro, Ocean Optics). In the case of testing the optical-electrochemical properties of the bifunctional device, the above experimental cell was replaced.

3. Results and discussion

ZnO nanorod arrays synthesized through an electrodeposition method on FTO substrates are used as the templates.[24] SEM images show that the electrodeposited ZnO exhibits well-aligned nanorod morphology and grows in tight contact with the FTO substrate (Fig. S1a and b†). An XRD pattern of these ZnO nanorod arrays shows that they are hexagonal ZnO crystals (JCPDS No. 36-1451) (Fig. S1c†). An ordered selected SAED pattern collected from a nanorod indicates its single-crystalline nature (Fig. S1d†). Additionally, large-area ZnO nanorod arrays can be easily prepared *via* this electrodeposition approach (Fig. S2†), making it possible to fabricate large-area TiO_2 nanotube arrays. After immersing the ZnO nanorod arrays in an aqueous solution consisting of $(NH_4)_2TiF_6$ and H_3BO_3 at room temperature for 30 min, amorphous titanium oxide nanotube arrays could be facilely obtained due to the STAH process. Post-annealing treatment led to the samples being fully crystallized. As shown in Fig. 2a and b, the as-prepared nanotube arrays exhibit a well-aligned structure, and adhere to the FTO substrate separately and strongly. The hollow structure can be clearly seen through the crack in a nanotube, where the red arrow points, in Fig. 2b. The typical lengths of the nanotubes are in the range of 150–500 nm, and the outer diameter is around 100 nm. The XRD patterns of the FTO substrate and the as-prepared nanotube arrays indicate the formation of anatase TiO_2 (JCPDS No. 21-1272) (Fig. 2c). The absence of diffraction peaks belonging to ZnO indicates that the templates are completely etched out during the STAH process, which can be further confirmed from Raman spectra of the FTO substrate, ZnO nanorod arrays, and TiO_2 nanotube arrays (Fig. S3†).

Owing to the fact that the hydrolysis reaction between TiF_6^{2-} and H_3BO_3 is rather slow,[22,23] it is believed that the size of the deposited TiO_2 particles should be very small, even on

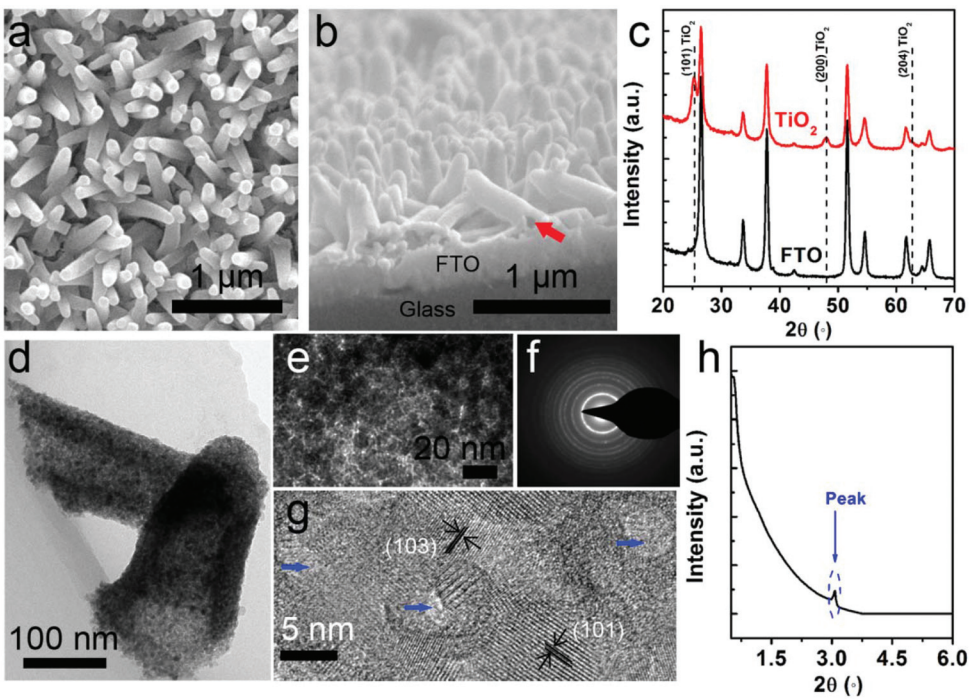

Fig. 2 (a) Top-view and (b) cross-sectional SEM images of the TiO_2 MNTAs. (c) XRD patterns of TiO_2 MNTAs and the FTO substrate. (d) and (e) bright-field TEM images of the TiO_2 MNTAs. (f) SAED pattern and (g) HRTEM image of one TiO_2 mesoporous nanotube. (h) Low-angle XRD pattern of the TiO_2 MNTAs.

the scale of a few nanometers. In addition, the random stacking of TiO_2 nanocrystals could lead the nanotubes to demonstrate a mesoporous nature. Fig. 2d shows a typical TEM image of nanotubes scraped from the FTO substrate, which confirms that the products are composed of 1D hollow nanotubes stacked with dense small particles. A magnified TEM image of the nanotubes confirms that the particles have a size of several nanometers (Fig. 2e). Such an ultrasmall TiO_2 particle size indicates that the TiO_2 MNTAs could exhibit high-rate electrochemical energy storage and a fast electrochromic response due to nanostructure-triggered rapid redox kinetics, including a possibly improved Li-ion diffusion coefficient and an enhanced pseudocapacitive effect.[16–18] Additionally, the TiO_2 nanoparticles are still strongly stacked together, even after the long sonication times involved in the preparation of the TEM specimen, implying their strong physical interactions, which are beneficial for good electron transport during redox processes. The distinct rings of the SAED pattern taken from the nanotube wall further illustrate the polycrystalline features of the nanotubes (Fig. 2f). Clear lattice fringes with intervals of approximately 0.35 and 0.24 nm, shown in a typical HRTEM image of the nanotubes, correspond to the lattice spacings of the (101) and (103) planes of anatase TiO_2 (Fig. 2g). The different exposed lattice planes among adjacent TiO_2 nanoparticles confirm the random stacking nature. Furthermore, as pointed to by the blue arrows in Fig. 2g, mesopores deriving from the random stacking of TiO_2 nanoparticles can be found. Fig. 2h exhibits the low-angle XRD pattern of TiO_2 nanotube arrays. The diffraction peak at 3.07° indicates the presence of mesopores with an average diameter of *ca.* 2.5 nm, while the weak intensity of this peak further confirms the irregular stacking of TiO_2 nanoparticles. Thus, it is concluded that the as-prepared TiO_2 MNTAs possess two kinds of pores, macropores derived from ZnO nanorods and mesopores formed by the random stacking of TiO_2 nanoparticles. Such hierarchical porous architecture favors good electrode/electrolyte contact. Although the scattering effects of a mesoporous structure could hinder visible light transmission to some extent, the as-prepared TiO_2 MNTA film still exhibits high transmission in the visible range (Fig. S4†). High transmission by the electrode film is beneficial for enhancing transmittance and color contrast between the colored and bleached states when the TiO_2 MNTAs are used to assemble electrochromic devices.[1–3]

Optical-electrochemical measurements were carried out to evaluate the lithium storage and electrochromic properties of the TiO_2 MNTA film electrodes. Cyclic voltammograms (CVs) within the range of −1.4–0.6 V *vs.* Ag/AgCl generally show a couple of redox peaks (Fig. 3a), corresponding to Li-ion insertion/extraction processes, which can be expressed as follows: $TiO_2 + xLi^+ + xe^- \leftrightarrow Li_xTiO_2$ ($x \leq 1$).[16,20] The increasing electrochemical polarization with the increase in scan rate causes the shift of the redox peaks. The TiO_2 MNTAs show a stable discharge specific capacity of *ca.* 176 mA h g^{-1} (corresponding to the Li-ion insertion for the anode material) and an acceptable charge specific capacity of 148 mA h g^{-1} (corresponding to the Li-ion extraction) at 0.75C (1C = 168 mA g^{-1}), leading to a Coulombic efficiency of 84% (Fig. S5†). When the current density goes up to a high current density of 15C, a high charge specific capacity of *ca.* 98 mA h g^{-1} is still maintained, with an increased Coulombic efficiency of 97% (Fig. 3b). More importantly, both the charge and discharge processes are completed in the short time range of 144–152 s, which is in the acceptable optical modulation response timescale for electrochromic applications, especially for smart windows,[1–6] implying the possible integration of high-rate capability with fast electrochromic response. Meanwhile, as shown in Fig. 3c and S6,† even at a ultrahigh current rate of 30 C, corresponding to 5.04 A g^{-1}, Li-ion insertion leads the TiO_2 MNTA film to exhibit a stable discharge capacity of 79 mA h g^{-1}, followed by almost complete Li-ion extraction, giving rise to a reversible charge

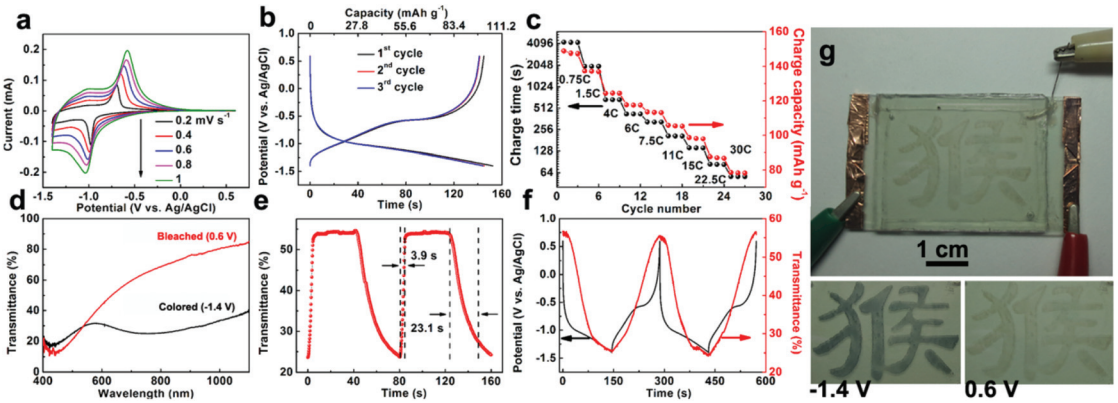

Fig. 3 (a) CV curves of TiO_2 MNTAs at different scan rates. (b) Galvanostatic charge/discharge curves of TiO_2 MNTAs at 15C. (c) Charge capacity and charging time of TiO_2 MNTAs at different current densities. (d) Transmittance contrast of TiO_2 MNTAs between 0.6 and −1.4 V. (e) Switching response curve of TiO_2 MNTAs under alternating voltages of 0.6 and −1.4 V at a wavelength of 700 nm. (f) Galvanostatic charge/discharge curves at 15C over the potential range of −1.4–0.6 V, and the corresponding *in situ* optical responses measured at 700 nm for the TiO_2 MNTA electrode. (g) Electrochromic device with an FTO/TiO_2/$LiClO_4$ + PC/FTO structure, using an Ag/AgCl wire as the reference electrode, and its color contrast at 0.6 and −1.4 V.

capacity of 78 mA h g^{-1} within a timescale of only 55 s. The high specific capacity and Coulombic efficiency obtained over short charge/discharge times verify the rapid and reversible Li^+ insertion/extraction kinetics, and superior rate performance of the TiO_2 MNTA film electrodes.

During ongoing CV or galvanostatic charge/discharge electrochemical process, electrochromism was observed in the TiO_2 MNTA film electrodes. Then, we investigated the electrochromic performance of TiO_2 MNTA film electrodes under chronoamperometric measurements over the same voltage range. As shown in Fig. 3d, at 0.6 V (*vs.* Ag/AgCl), the electrode exhibits continuous transmittance, increasing from 13.2% at 450 nm to 65% at 750 nm, leading to a nearly transparent state. Li-ion insertion under a cathodic potential of −1.4 V causes a relatively homogeneous transmission of 24% in the visible spectrum range, except for a small peak at 570 nm, leading to deep blue coloration. High transmittance modulation of *ca*. 33.5% is achieved at a typical wavelength of 700 nm between 0.6 and −1.4 V. A second important electrochromism performance marker is the switching response under alternating potentials (−1.4 and 0.6 V). When the coloration and bleaching times are defined as the times required for a 90% change in full transmittance modulation,[25] the TiO_2 MNTA film electrode demonstrates a fast bleaching response of 3.9 s and a moderate coloration response of 23.1 s (Fig. 3e). The bleaching/coloration response speed of the TiO_2 MNTA film electrode is comparable to that of anodic TiO_2 nanotube electrode films with ultrathin wall thickness,[26,27] but much faster than that of TiO_2 nanorod array electrode films prepared *via* hydrothermal methods.[28,29]

As shown in the aforementioned separate tests on energy storage and electrochromism, it can be concluded that the TiO_2 MNTA film electrodes exhibit high rate capacity achieved in a short charge/discharge time, and high transmittance modulation accompanying a fast switching response. To further prove that the electrodes are suitable for the assembly of electrochromic energy storage devices, the *in situ* transmittance response of the TiO_2 MNTA film electrode during the charge/discharge process at a current density of 15C at 700 nm was tested. The discharge and charge capacities are derived from the insertion and extraction of Li-ions into and out of the TiO_2 nanocrystals, leading to reversible Ti valence changes between +4 and +3. Such valence changes in turn give rise to reversible transmittance changes (Fig. 3f), as well as the vivid color contrast demonstrated by the electrochromic cell (Fig. 3g).

As for the Li-ion insertion profiles of anatase TiO_2, the constant voltage plateau represents a sluggish phase transformation-based redox process, where the anatase and lithium titanate phases coexist, while the slope curves demonstrate the fast capacitive energy storage manner of a single-phase material.[8,16,18] As shown in Fig. S5,† the short two-phase region observed at 0.75C indicates that the major redox process of the TiO_2 MNTA electrode is capacitive, usually leading to high-rate capability and a fast electrochromic response.[16,25,30,31] To reveal the enhancement due to structural modification towards the Li-ion insertion process, we investigated the redox kinetics of the TiO_2 MNTAs using analytical approaches that take advantage of the differences between diffusion and capacitive redox processes. The capacitive effect can be characterized by analyzing CV data at various scan rates. Assuming that the redox current (i) obeys a power-law relationship to the scan rate (v) leads to the relationship $i = av^b$,[8,16] where a and b are adjustable values. When the value of b is 0.5, the current response is diffusion-controlled (intercalative), whereas a value of 1 indicates that the current is surface-controlled (capacitive). The calculated b-values for TiO_2 MNTAs between −0.75 and −1.25 V during the cathodic scan process are shown in Fig. 4a. At a peak potential of −0.95 V, the b-value is 0.56, indicating that the current comes primarily from the Li-ion insertion reaction. At potentials higher or lower than the peak potential, b-values are in the range of 0.8–1.0, indicating that the current is predominantly capacitive. For Li-ion extraction during an anodic scan between −0.11 and −0.4 V (Fig. 4b), it is also found that the capacitive current response makes a major contribution, while phase transformation-based current appears only in the voltage range around the anodic peak. Thus, it can be concluded that Li-ion redox in TiO_2 MNTAs is feasible.[8,16–18]

A closer examination of the voltammetric scan rate dependence enables one to distinguish quantitatively the capacitive contribution to the current response. For a specific CV scanning rate (v), the measured current (i) at a fixed potential (V) can be quantitatively separated into capacitive (k_1v) and diffusion-controlled ($k_1v^{1/2}$) responses, according to $i(V) = k_1v + k_1v^{1/2}$.[8,16] By determining k_1 and k_2, one can distinguish between intercalation storage and energy storage from capacitance. As shown in Fig. 4c, the diffusion-controlled charge in the TiO_2 MNTAs is mainly generated around the peak voltage, further indicating that the diffusion process is feasible in this region. Based on quantification at 0.4 mV s^{-1}, as much as approximately 51.4% of the total current (therefore, the capacitance) is capacitive. The capacitive capacity is improved gradually upon increasing the scan rate, and finally reaches 61.5% at 1 mV s^{-1} (Fig. 4d). Such a high capacitance contribution undoubtedly indicates the importance of an enhanced surface redox contribution to the high-rate energy storage and fast electrochromic response in the TiO_2 MNTA film electrodes.

In addition, the b-value of the TiO_2 electrode near the redox peak is 0.56, implying that Li-ion insertion occurs. To further investigate the influence of the as-formed nanostructure on the Li-ion insertion kinetics in TiO_2 MNTAs, the Li-ion diffusion coefficient (D_{Li}) was evaluated *via* a chronocoulometric method, according to the equation: $Q = 2n^{-1/2}FAD_{Li}^{1/2}C_0t^{1/2} + Q_{dl} + nF\Lambda\Gamma$,[21,32] where Q is the integrated charge, n is the number of electrons transferred in redox reactions, A is the electrode area, D_{Li} is the Li^+ chemical diffusion coefficient, C_0 is the Li^+ surface concentration, Q_{dl} is the double-layer charge, F represents the Faraday constant, and Γ is the concentration of adsorbed species during the faradaic reaction. Fig. 4e and f show the current response curve of the TiO_2 MNTA film when the voltage was switched from 0.5 V to −1.3 V, and the corres-

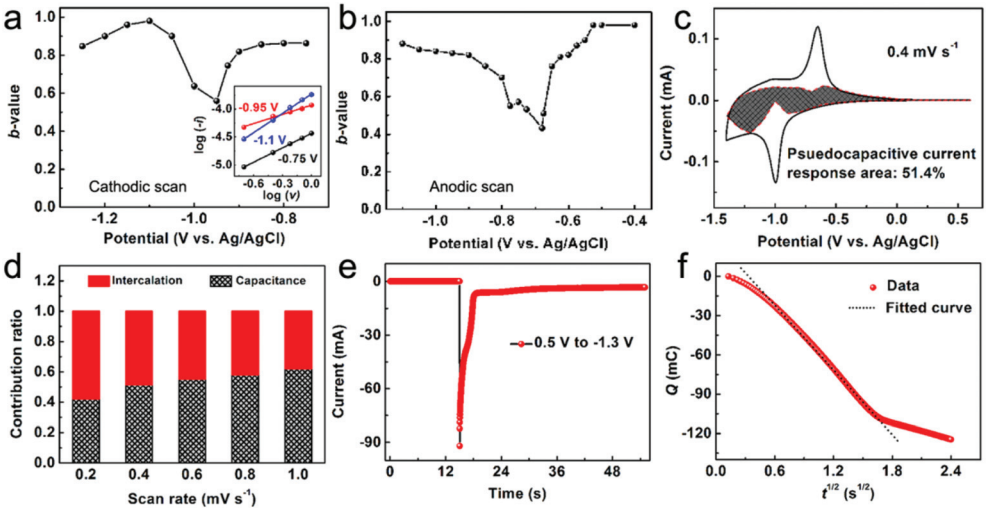

Fig. 4 The *b*-values of the TiO_2 MNTAs plotted as a function of potential for (a) the cathodic scan (Li-ion insertion) and (b) the anodic scan (Li-ion extraction); inset: the power law dependence of current on sweep rate shows good linearity at three typical potentials, −0.75 V, −0.95 V, and −1.1 V. (c) The separation of the capacitive and diffusion currents in TiO_2 MNTAs at 0.4 mV s^{-1}. The capacitive contribution is shaded. (d) The contribution ratio for the capacitive and diffusion-controlled charge *versus* scan rate. (e) The chronoamperometric response curve of the TiO_2 MNTAs from 0.5 V to −1.3 V, and (f) corresponding plots of *Q vs.* $t^{1/2}$.

ponding plot of *Q vs.* $t^{1/2}$, respectively. The calculated D_{Li} value of the TiO_2 MNTAs is 8.8×10^{-15} cm^2 s^{-1}, which is much higher than that of CVD-prepared TiO_2 film (2×10^{-15} cm^2 s^{-1}) and sol–gel-prepared TiO_2 nanoporous film (1×10^{-15} cm^2 s^{-1}), detected using the same electroanalytical method and electrolyte.[21] The improved D_{Li} value also influences positively the Li-ion storage performance of the TiO_2 MNTA film, since a higher D_{Li} value can result in accelerated Li-ion diffusion, thus enabling more Ti^{4+} ions to take part in redox reactions.

Energy storage smart windows, for practical applications, are expected to exhibit fast and reversible transmittance modulation with high-rate electrochemical energy storage under a chronopotentiometric operation model, that is, a galvanostatic charge/discharge process. In CV tests, the bifunctional smart window exhibits deep blue coloration, as well as a redox current response and transmittance modulation over a voltage range from −2.4 to −4.0 V (Fig. 5a), indicating the occurrence of Ti^{4+}/Ti^{3+} redox over this voltage range. The symmetric char-

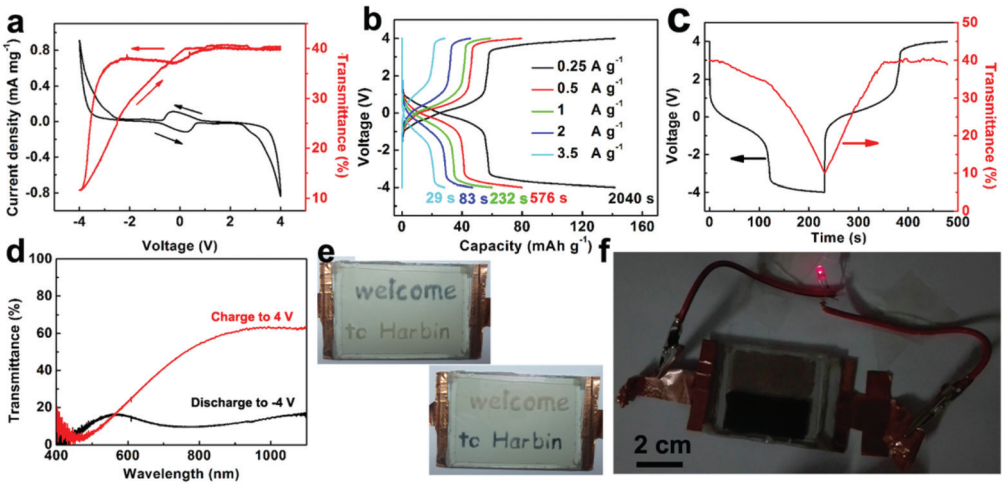

Fig. 5 (a) The optical transmittance response at λ = 700 nm as a function of the applied potential, and the corresponding *CV* curve recorded at a scan rate of 2 mV s^{-1} over the potential range from −4 to 4 V. (b) Galvanostatic charge/discharge curves of the bifunctional device at different current densities. (c) Galvanostatic charge/discharge curves at 1 A g^{-1} and the corresponding *in situ* optical responses measured at 700 nm for the bifunctional device. (d) and (e) The transmittance and color contrast of the bifunctional device between −4.0 and 4.0 V. (f) An optical image of a fully charged bifunctional device powering a red LED.

acter of the CV curves confirms the symmetric structure of the bifunctional device. Voltages beyond ±4.0 V cause the appearance of redox in the FTO substrate layer, leading to irrecoverable damage to the device. Galvanostatic charge/discharge curves from the device between +4.0 and −4.0 V were collected at different current densities (Fig. 5b). At a current density of 0.25A g^{-1}, the assembled bifunctional smart window delivers a discharge specific capacity of 142 mA h g^{-1} within 2040 s. When the current density goes up to 1 A g^{-1}, a shorter time of 232 s is needed to complete the discharge process, and the device can still deliver a high discharge specific capacity of 60 mA h g^{-1}. *In situ* optical measurements were used to monitor transmittance modulation during the galvanostatic charge/discharge process. As shown in Fig. 5c and d, the device exhibits high transmittance modulation of *ca.* 30.4% at 700 nm, as well as obvious transmittance contrast over the whole visible spectrum range between the charged state and discharged state at 1 A g^{-1}. Furthermore, upon wisely designing the pattern of the TiO_2 MNTA film, the bifunctional electrochromic device can show interesting display contrast (Fig. 5e). The fabricated device also exhibits high cycling durability. The degradation of the discharge capacity and transmittance modulation is only 4 mA h g^{-1} and 1%, respectively, at 1 A g^{-1} after 200 cycles (Fig. S7†). This device also presents fast transmittance modulation over the whole spectrum range, an acceptable discharge capacity of 47 mA h g^{-1}, and obvious color changes within a short discharge time of 83 s at a high charge/discharge current density of 2 A g^{-1} (Fig. S8†). Even at 3.5 A g^{-1}, the assembled device still maintains an acceptable discharge capacity of 29 mA h g^{-1} within an ultrashort discharge time of 29 s. When the assembled device is fully charged under a current density of 1 A g^{-1}, a red LED can be lit (Fig. 5f), indicating broad applications as a power supply when used in green energy-efficient buildings.

4. Conclusions

In summary, we have demonstrated a bifunctional smart window with rapid Li-ion redox kinetics and desirable energy capacity based on TiO_2 mesoporous nanotube array (MNTA) film electrodes. The nanotube arrays were prepared *via* a sacrificial template-accelerated hydrolysis strategy, and demonstrated mesoporous walls constructed through the stacking of several nanometer-sized TiO_2 nanocrystals. Optical-electrochemical measurements demonstrated that the TiO_2 MNTAs simultaneously exhibited high specific capacity and desirable optical modulation over a short charge/discharge time. Electrochemical analysis indicated that rapid Li-ion insertion kinetics, including an enhanced pseudocapacitive effect and Li-ion diffusion coefficient, is the main origin of this. Upon assembling a designed sandwich-like structure, a bifunctional smart window exhibited desirable transmittance modulation with obvious color changes (deep blue/transparent) and high-rate capability over short galvanostatic charge/discharge times. We believe that the assembled electrochromic device could not only function as a smart window, but could also concurrently power electronic devices, such as LEDs and sensors, leading to profound impacts on our daily life in the future.

Conflicts of interest

There are no conflicts to declare.

Acknowledgements

We thank the National Natural Science Foundation of China (No. 51572058, 51502057), the National Key Research & Development Program (2016YFB0303903), the Foundation of Science and Technology on Advanced Composites in Special Environment Laboratories, the Science and Technology Foundation of the Guizhou Province of China (No. qian ke he ji chu [2017] 1065), the Scientific Research Starting Project of SWPU (2017QHZ019), and the Young Scholars Development Fund of SWPU (201799010003).

Notes and references

1 A. Azens and C. Granqvist, *J. Solid State Electrochem.*, 2003, **7**, 64–68.
2 V. K. Thakur, G. Ding, J. Ma, P. S. Lee and X. Lu, *Adv. Mater.*, 2012, **24**, 4071–4096.
3 R. Baetens, B. P. Jelle and A. Gustavsend, *Sol. Energy Mater. Sol. Cells*, 2010, **94**, 87–105.
4 C. G. Granqvist, *Sol. Energy Mater. Sol. Cells*, 2013, **99**, 1–13.
5 A. Llordés, G. Garcia, J. Gazquez and D. J. Milliron, *Nature*, 2013, **500**, 323–326.
6 M. R. J. Scherer, L. Li, P. M. S. Cunha, O. A. Scherman and U. Steiner, *Adv. Mater.*, 2012, **24**, 1217–1221.
7 Z. Tong, Y. Tian, H. Zhang, X. Li, J. Ji, H. Qu, N. Li, J. Zhao and Y. Li, *Sci. China: Chem.*, 2017, **60**, 13–37.
8 V. Augustyn, P. Simon and B. Dunn, *Energy Environ. Sci.*, 2014, **7**, 1597–1614.
9 P. Yang, P. Sun and W. Mai, *Mater. Today*, 2016, **19**, 394–402.
10 D. Wei, M. R. J. Scherer, C. Bower, P. Andrew, T. Ryhänen and U. Steiner, *Nano Lett.*, 2012, **12**, 1857–1862.
11 K. Wang, H. Wu, Y. Meng, Y. Zhang and Z. Wei, *Energy Environ. Sci.*, 2012, **5**, 8384–8389.
12 P. Yang, P. Sun, Z. Chai, L. Huang, X. Cai, S. Tan, J. Song and W. Mai, *Angew. Chem., Int. Ed.*, 2014, **53**, 11935–11939.
13 J. Wang, L. Zhang, L. Yu, Z. Jiao, H. Xie, X. W. Lou and X. W. Sun, *Nat. Commun.*, 2014, **5**, 4921.
14 J. Zhao, Y. Tian, Z. Wang, S. Cong, D. Zhou, Q. Zhang, M. Yang, W. Zhang, F. Geng and Z. Zhao, *Angew. Chem., Int. Ed.*, 2016, **55**, 7161–7165.
15 Z. Tong, J. Hao, K. Zhang, J. Zhao, B. Su and Y. Li, *J. Mater. Chem. C*, 2014, **2**, 3651–3658.

16 S. Lou, X. Cheng, Y. Zhao, A. Lushington, J. Gao, Q. Li, P. Zuo, B. Wang, Y. Gao, Y. Ma, C. Du, G. Yin and X. Sun, *Nano Energy*, 2017, **34**, 15–25.
17 Z. Tong, H. Xu, G. Liu, J. Zhao and Y. Li, *Electrochem. Commun.*, 2016, **69**, 46–49.
18 T. Brezesinski, J. Wang, J. Polleux, B. Dunn and S. H. Tolbert, *J. Am. Chem. Soc.*, 2009, **131**, 1802–1809.
19 K. Lee, D. Kim, S. Berger, R. Kirchgeorg and P. Schmuki, *J. Mater. Chem.*, 2012, **22**, 9821–9825.
20 R. Mo, Z. Lei, K. Sun and D. Rooney, *Adv. Mater.*, 2014, **26**, 2084–2088.
21 H. Lindström, S. Södergren, A. Solbrand, H. Rensmo, J. Hjelm, A. Hagfeldt and S. Lindquist, *J. Phys. Chem. B*, 1997, **101**, 7710–7716.
22 J. Lee, I. Leu, M. Hsu, Y. Chung and M. Hon, *J. Phys. Chem. B*, 2005, **109**, 13056–13059.
23 J. Liu, Y. Li, H. Fan, Z. Zhu, J. Jiang, R. Ding, Y. Hu and X. Huang, *Chem. Mater.*, 2010, **22**, 212–217.
24 X. Lu, G. Wang, S. Xie, J. Shi, W. Li, Y. Tong and Y. Li, *Chem. Commun.*, 2012, **48**, 7717–7719.
25 Z. Tong, N. Li, H. Lv, Y. Tian, H. Qu, X. Zhang, J. Zhao and Y. Li, *Sol. Energy Mater. Sol. Cells*, 2016, **146**, 135–143.
26 S. Berger, A. Ghicov, Y.-C. Nah and P. Schmuki, *Langmuir*, 2009, **25**, 4841–4844.
27 H. Lv, N. Li, H. Zhang, Y. Tian, H. Zhang, X. Zhang, H. Qu, C. Liu, C. Jia, J. Zhao and Y. Li, *Sol. Energy Mater. Sol. Cells*, 2016, **150**, 57–64.
28 J. Chen, W. Ko, Y. Yen, P. Chen and K. Lin, *ACS Nano*, 2012, **6**, 6633–6639.
29 P. Qiang, Z. Chen, P. Yang, X. Cai, S. Tan, P. Liu and W. Mai, *Nanotechnology*, 2013, **24**, 435403.
30 V. Augustyn, J. Come, M. A. Lowe, J. Kim, P. Taberna, S. H. Tolbert, H. D. Abruña, P. Simon and B. Dunn, *Nat. Mater.*, 2013, **12**, 518–522.
31 V. Augustyn, E. R. White, J. Ko, G. Grüner, B. C. Regan and B. Dunn, *Mater. Horiz.*, 2014, **1**, 219–223.
32 Z. Tong, H. Yang, L. Na, H. Qu, X. Zhang, J. Zhao and Y. Li, *J. Mater. Chem. C*, 2015, **3**, 3159–3166.